Compact Wireless Energy Pick-Up System Coupled Gate-Drive for Medium-Voltage Power Devices in Modular DC Solid-State Circuit Breakers

Shuyan Zhao, *Student Member, IEEE*, Yao Wang, *Student Member, IEEE*, Reza Kheirollahi, *Student Member, IEEE*, Yang Zheng, Zilong Zheng, Shervin Salehi Rad, Hua Zhang, *Member, IEEE*, and Fei Lu, *Member, IEEE*

***Abstract*—This article presents a compact inductive power transfer (IPT) based wireless energy pick-up system (WEPUS) coupled gate-drive for medium-voltage power devices in modular direct current (dc) solid-state circuit breakers (SSCBs). There are two major contributions. First, an *LCL-S* compensated IPT system with constant voltage outputs is applied as auxiliary power supply to power ten submodules in SSCBs, which is advantageous in terms of load independence. Second, a compact modular WEPUS is integrated as part of a power electronics building block (PEBB) to provide modularity in SSCBs. A WEPUS prototype is implemented for ten loads to test power transfer performance, which achieves a peak dc-to-dc efficiency of 88.2% at 47.1 W and 230 kHz frequency. Then, the WEPUS is installed on a real SSCB prototype with ten parallel PEBBs. A 400 A/1 h dc continuous test and a 2 kA fault interruption test powered by the WEPUS are performed, which validate the proposed WEPUS to support SSCBs in both steady-state and transient interruption working modes. This article is accompanied by a slide as multimedia material demonstrating the contributions of the presented work.**

***Index Terms*—Inductive power transfer (IPT), modularity, power electronics building block (PEBB), solid-state circuit breaker (SSCB).**

I. Introduction

MODERN direct current (dc) power system has been witnessing rapid development for the sake of efficiency [1], [2], [3], power density [4], and renewable penetration [5], which is of great significance for carbon neutrality. However, due to the nonexistence of natural current zero crossings and low fault impedance, dc circuit breakers are required to achieve reliable and fast protection [6].

Manuscript received 1 April 2023; revised 6 June 2023; accepted 1 July 2023. Date of publication 5 July 2023; date of current version 1 September 2023. This work was funded in part by the Advanced Research Projects Agency-Energy (ARPA-E), U.S. Department of Energy, under Award Number DE-AR0001114 in the BREAKERS program monitored by Dr. Isik Kizilyalli. Recommended for publication by Associate Editor M. Liu. *(Corresponding author: Fei Lu.)*

Shuyan Zhao, Yao Wang, Reza Kheirollahi, Yang Zheng, Zilong Zheng, Shervin Salehi Rad, and Fei Lu are with the Department of Electrical and Computer Engineering, Drexel University, Philadelphia, PA 19104 USA (e-mail: sz568@drexel.edu; yw696@drexel.edu; rk887@drexel.edu; cz426@drexel.edu; zz529@drexel.edu; ss5485@drexel.edu; fei.lu@drexel.edu).

Hua Zhang is with the Department of Electrical and Computer Engineering, Rowan University, Glassboro, NJ 08028 USA (e-mail: zhangh@rowan.edu).

This article has supplementary material provided by the authors and color versions of one or more figures available at https://doi.org/10.1109/TPEL.2023.3292365.

Digital Object Identifier 10.1109/TPEL.2023.3292365

Recently, solid-state circuit breakers (SSCBs) can realize fast response and arc-free breaking features compared to traditional mechanical or hybrid circuit breakers [7], which is superior for aerospace, navy vessels, electric vehicle charging stations, and solar farms [8]. With the development of medium voltage wide bandgap devices, new opportunities for SSCBs are promising with high ratings and efficiency. However, due to the semiconductor on-state resistance compared to a metal contactor, it is necessary to package multiple devices in parallel [9]. Modular design concept [10] has been proven as an effective solution to achieve high current rating and efficiency. Realizing modular auxiliary power supply (APS) for gate drive is a major technical challenge. As the enhanced operation rating of modern medium-voltage power devices, it is motivated to develop new technologies of isolated APS for gate-drive designs to achieve better modularity, robustness, safety, and reliability, thence facilitating the development of the oriented SSCB applications.

Domino-type inductive power transfer (IPT) relay system has been investigated to provide constant current (CC) or constant voltage (CV) outputs [11], [12], [13], [14], [15], [16], [17], [18]. Different compensations from simple series/parallel to high-order T- or π-type networks [19] have been proposed. Cheng et al. [11] presents an S-SP compensated IPT relay system with six CV outputs using asymmetrical coils. A five-stage double-output IPT system with CV outputs is proposed in [12], which features cylindrical solenoid couplers for insulator applications. Chen et al. [13] proposes a bilateral excitation based a domino IPT system with eight outputs to improve load independence and efficiency.

However, there are drawbacks in the domino IPT solutions. As shown in Fig. 1, the configuration of the last receiver unit is different from others [14], [15], [16], [17], [18], affecting modularity in mass production. To reduce cross couplings between non-adjacent units while maintaining main couplings, a relatively large bipolar double-D coil layout is usually used, which reduces power density. Besides, there is an output voltage drop in each relay unit due to inevitable parasitic resistance, which limits the maximum number of power transfer units.

Single-transmitter-multiple-receiver APS is a mainstream solution. Existing designs in [20], [21], [22], [23], and [24] adopt

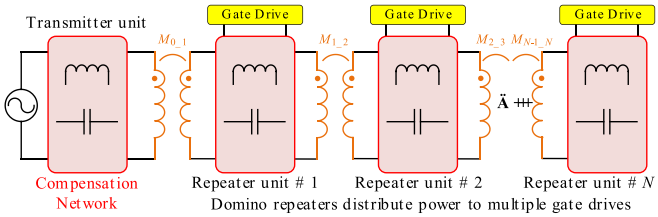

Fig. 1. Existing domino IPT system for gate drives, achieving load independent CV outputs, but losing modularity and consistency with cross couplings.

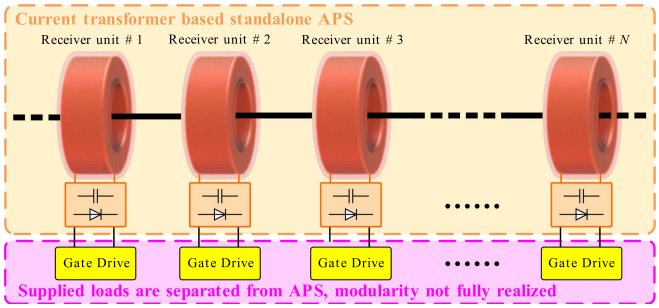

Fig. 2. Existing CT-based APS, which lacks investigations on output number, efficiency, load-independent CV outputs and modularity.

similar schemes, which use a large primary coil and multiple smaller receiver coils. However, cross couplings and magnetic field uniformness between receivers are critical concerns.

Fig. 2 shows a general configuration of current transformer (CT) based APS. The authors in [25], [26], and [27] adopt it to supply power to gate drivers. However, maximum output number and efficiency are not optimized in these designs, neither the load-independent CV characteristic is investigated. The idea of modular design is still not realized in these standalone APS systems.

To overcome the technical gaps, this article proposes a novel CT-based wireless energy pick-up system (WEPUS) for SSCB APS applications. It features high efficiency and low voltage regulation over a wide load range. There are two major contributions.

1) A single-transmitter multireceiver LCL-S compensated IPT system with ten CV outputs is implemented for real SSCB gate drivers for the first time.
2) Good compactness and complete modularity are achieved. Identical APS pick-up units are installed into each power electronics building block (PEBB) submodule, realizing a modular SSCB.

For the sake of disambiguation, it must be noticed that the efficiency of the proposed WEPUS APS is different from the SSCB efficiency in this article.

II. Proposed Wireless Energy Pick-Up System

A. System Description

Fig. 3 shows the proposed WEPUS system with N outputs. An LC compensation network is applied to achieve a CC in the primary track, which consists of an inductor L_1 and a capacitor C_1. All pick-up units receive power from the same track, which has an inductance of L_p. A series compensation C_s is used at the secondary side to achieve load independent CV outputs. With $n = 1, 2, \ldots, N$, the mutual coupling between the primary track and pick-up coils is M_n, the pick-up coil inductance is L_{sn}, the compensation capacitor is C_{sn}, and the load resistance is R_{Ln}.

B. Circuit Working Principle Analysis

In Fig. 3, the coupling coefficient k_n is defined as

$$k_n = M_n \Big/ \sqrt{L_p L_s},\ n = 1, 2, \cdots N. \tag{1}$$

Fig. 4 shows the equivalent circuit of the proposed WEPUS with N loads. The input voltage V_{in}, input current I_1, track current I_p, and pick-up current I_{sn} are also provided. The input voltage V_{in} is given as

$$V_{\text{in}} = 2\sqrt{2}V_{\text{dc}} \Big/ \pi. \tag{2}$$

Quality factors of coils are defined as

$$Q_1 = \omega L_1/r_1, Q_p = \omega L_p/r_p, Q_{sn} = \omega L_{sn}/r_{sn}, n = 1, 2, \ldots, N \tag{3}$$

r_1, r_p and r_{sn} represent parasitic resistances, the angular frequency is defined as ω_0, and resonances are expressed as

$$\omega_0 L_1 = \omega_0 L_p = 1/\omega_0 C_1, \omega_0 L_{sn} = 1/\omega_0 C_{sn}, n = 1, 2, \ldots, N. \tag{4}$$

The pick-up unit impedance Z_{sn} are described as

$$Z_{sn} = j\omega L_{sn} + 1/j\omega C_{sn} + r_{sn} + R_{Ln}, n = 1, 2, \ldots, N. \tag{5}$$

Based on Fig. 4 and (5), the reflected impedance of each unit Z_{pn} and total reflection impedance Z_p at the primary side are

$$Z_p = \sum_{n=1}^{N} Z_{pn}, Z_{pn} = (\omega M_n)^2 \Big/ Z_{sn}, n = 1, 2, \ldots, N. \tag{6}$$

The input impedance of the system is depicted

$$Z_{\text{in}} = r_1 + j\omega L_1 + 1 \Big/ \left(j\omega C_1 + \frac{1}{j\omega L_p + r_p + Z_p}\right). \tag{7}$$

At resonance, Z_{in} becomes resistive, as described in (8). It means the proposed WEPUS achieves zero phase angle (ZPA)

$$Z_{\text{in}} = r_1 + (\omega L_1)^2 \Big/ (r_p + Z_p). \tag{8}$$

The input current I_1, track current I_p, and pick-up unit current I_{sn} are depicted as

$$\begin{cases} I_1 = \frac{V_{\text{in}}}{Z_{\text{in}}}, I_p = I_1 \frac{1/j\omega C_1}{1/j\omega C_1 + j\omega L_p + r_p + Z_p} \\ I_{sn} = j\omega M_n I_p / Z_{sn}, n = 1, 2, \ldots, N \end{cases}. \tag{9}$$

At resonance, the currents can be simplified as

$$\begin{cases} I_1 = \frac{V_{\text{in}}}{r_1 + (\omega L_1)^2/(r_p + Z_p)}, I_p = \frac{-j\omega L_1 V_{\text{in}}}{r_1(r_p + Z_p) + (\omega L_1)^2} \\ I_{sn} = \frac{-\omega^2 L_1 M_n V_{\text{in}}}{Z_{\text{in}} Z_{sn}(r_p + Z_p)}, n = 1, 2, \ldots, N \end{cases}. \tag{10}$$

The induced voltage on the pick-up unit is derived as

$$V_{Ln} = \frac{j\omega M_n I_p R_{Ln}}{r_{sn} + R_{Ln}} = \frac{\omega^2 L_1 M_n V_{\text{in}} R_{Ln}}{(r_{sn} + R_{Ln})\left[r_1(r_p + Z_p) + (\omega L_1)^2\right]}. \tag{11}$$

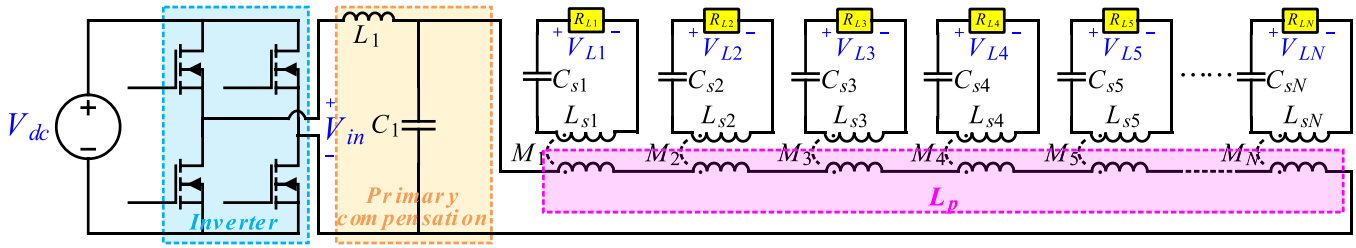

Fig. 3. Proposed WEPUS system with *LCL-S* compensation, powering *N* loads.

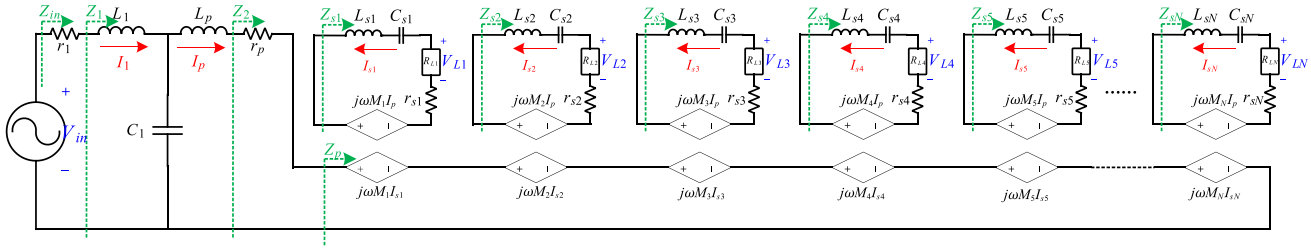

Fig. 4. Behavior sources based equivalent circuit model of the proposed WEPUS system with *N* loads, including parasitic resistances of coils.

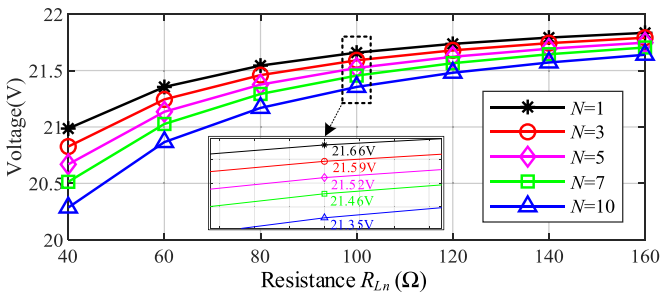

Fig. 5. Calculated output voltages versus load resistance R_{Ln} at different numbers of output *N* (k=0.2, Q_1=Q_p=50, and Q_{sn}=100).

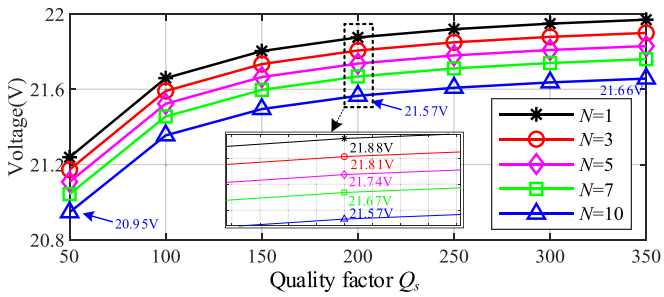

Fig. 6. Calculated output voltages versus quality factor of receiver coils Q_s at different numbers of output *N* (k=0.2, Q_1=Q_p=50, and R_{Ln}=100 Ω).

Assuming parasitic resistances of L_1 and L_{sn} are negligible, the track current I_p and output voltage V_{Ln} are derived as

$$|I_p| \approx \frac{V_{\text{in}}}{\omega L_1}, |V_{Ln}| \approx \frac{M_n}{L_1} \cdot V_{\text{in}}. \tag{12}$$

It reveals that the primary track has a CC, which helps to induce CV on the pick-up units. By tuning parameters to achieve $M_1 = M_2 = \cdots = M_n$, the consistency of outputs can be realized.

C. Sensitivity Analysis of Voltage Outputs

In the following calculations, the dc input voltage V_{dc} is set as 18 V, the frequency selected as 230 kHz, primary track inductance $L_p = 3$ μH, and receiver inductance $L_s = 140$ μH. Identical inductances, and load resistances are used, namely $L_{s1} = L_{s2} = \cdots = L_{sN}$, $M_1 = M_2 = \cdots = M_N$, and $R_{L1} = R_{L2} = \cdots = R_{LN}$. Compensation capacitors are calculated according to (4).

Fig. 5 shows the variation of output voltages with load R_{Ln}, which is calculated based on $k = 0.2$, $Q_1 = Q_p = 50$, and $Q_{sn} = 100$. As the WEPUS supplies more units, the output voltage decreases. For example, when $R_{Ln} = 100$ Ω, the output voltage reduces from 21.66 to 21.36 V as *N* increases from 1 to 10. It is because the increased total reflected impedance Z_p based on (6) can lead to a voltage reduction based on (11). It also explains that the load-independent CV characteristic is impacted as *N* increases.

Fig. 6 shows the variation of output voltages with Q_{sn}, which is calculated based on $k = 0.2$, $Q_1 = Q_p = 50$, and $R_{Ln} = 100$ Ω. As Q_{sn} increases, the voltage drop on the parasitic resistance reduces, and output voltages increase. It also indicates that keeping increasing Q_{sn} becomes less effective. For example, when $N = 10$, the voltage increment is 0.62 V as Q_{sn} increases from 50 to 200, which is much more significant than that of only 0.09 V as Q_{sn} further increases from 200 to 350.

Regarding the oriented application, it is desired to achieve modularity of the SSCB gate-drive, which means that it needs to be acceptable to adjust total number of output units *N* (SSCB submodules) without changing any design parameters including the WEPUS system. It gives better flexibility to facilitate the design process of SSCBs targeting different application situations. Specifically, Figs. 5 and 6 show the simulated performance of the

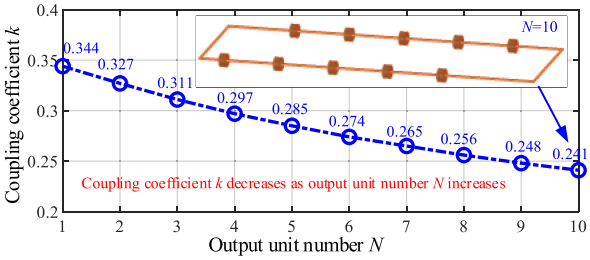

Fig. 7. Maxwell-simulated coupling coefficient k versus output unit number N.

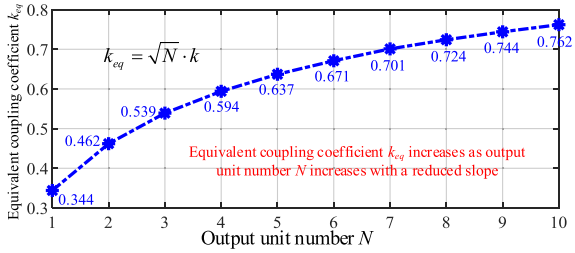

Fig. 8. Calculated equivalent coupling coefficient k_{eq} versus output unit number N.

WEPUS system at number of output circuits spanning from $N = 1$ to $N = 10$ while keeping same circuit parameters. It indicates that the desired CV outputs is achieved even with the output number N varying in such a wide range.

D. Output Efficiency Analysis

Fig. 7 shows the Maxwell-simulated coupling coefficient k at different output units number N. The coupler design details will be demonstrated in Section III-A. It indicates that k decreases as N increases due to the increment of primary track inductance L_p. Specifically, when $N = 10$, $k = 0.241$ which drops significantly compared to $k = 0.344$ at $N = 1$.

In a traditional one-to-one IPT systems, reduction of k means decreasing of efficiency, as shown by (13) revealed in [28]

$$\eta_{\text{coupler(1to1)}} = \frac{1}{1 + \frac{1}{\alpha_L} + \frac{1}{k^2 Q_p Q_{sn}}\left(\frac{1}{\alpha_L} + \alpha_L + 2\right)},$$
$$\alpha_L = \frac{R_{\text{Load}}}{r_s}. \tag{13}$$

However, for a one-to-N system in this article, based on Fig. 4, the coupler efficiency (coil to coils) is provided as

$$\eta_{\text{coupler(1to}N\text{)}} = \frac{N I_{sn}^2 R_{Ln}}{I_p^2 r_p + N I_{sn}^2 r_{sn} + N I_{sn}^2 R_{Ln}} = \frac{1}{\left(\frac{I_p}{I_{sn}}\right)^2 \frac{r_p}{N R_{Ln}} + \frac{r_{sn}}{R_{Ln}} + 1}. \tag{14}$$

Defining a receiving side load coefficient as $\alpha_L = R_{Ln}/r_{sn}$, the system efficiency can be further derived as

$$\eta_{\text{coupler(1to}N\text{)}} = \frac{1}{1 + \frac{1}{\alpha_L} + \frac{1}{k^2 Q_p Q_{sn} N}\left(\frac{1}{\alpha_L} + \alpha_L + 2\right)}. \tag{15}$$

It can be further simplified as

$$\eta_{\text{coupler(1to}N\text{)}} = \frac{1}{1 + \frac{1}{\alpha_L} + \frac{1}{k_{\text{eq}}^2 Q_p Q_{sn}}\left(\frac{1}{\alpha_L} + \alpha_L + 2\right)},$$
$$k_{\text{eq}} = \sqrt{N} \cdot k \tag{16}$$

k_{eq} is defined as the equivalent coupling coefficient that relates to N. Equation (16) is similar to (13), implying intrinsic similarities between single-load and multiload systems. It indicates that the efficiency depends on the quality factor and the equivalent coupling coefficient k_{eq}.

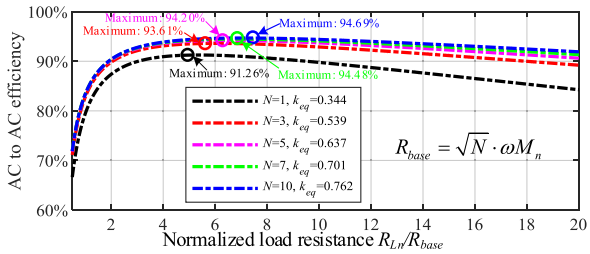

Fig. 9. Calculated AC-to-AC efficiency versus normalized load resistance at different numbers of output N.

Fig. 8 shows calculated equivalent coupling coefficient k_{eq} based on Maxwell simulated results in Fig. 7. It implies that k_{eq} increases as N increases with a reduced slope.

The maximum coupler efficiency and corresponding optimal load resistance are then derived as shown in

$$\begin{cases} \eta_{\text{coupler\_max}} = \dfrac{k_{\text{eq}}^2 Q_p Q_{sn}}{\left(1 + \sqrt{k_{\text{eq}}^2 Q_p Q_{sn} + 1}\right)^2} \\ R_{Ln\_\text{optimal}} = \sqrt{N} \cdot \omega M_n \sqrt{\frac{r_{sn}}{r_p}} \end{cases}. \tag{17}$$

The parameter normalization is used to normalize load resistances. In [28], the base value is defined as below. The normalized load resistance is defined as R_{Ln}/R_{base}

$$R_{\text{base}} = \sqrt{N} \cdot \omega M_n. \tag{18}$$

The optimal normalized load is then derived as

$$R_{Ln\_\text{optimal}}/R_{\text{base}} = \sqrt{r_{sn}/r_p}. \tag{19}$$

Equation (19) can be used as a design guidance to match the gate-drive load in real applications for the sake of simplicity.

Fig. 9 further shows the MATLAB calculated ac-to-ac efficiency with normalized load by impedance analysis as

$$\eta_{\text{IPT}} = \frac{|Z_1|}{|Z_{\text{in}}|}\eta_{\text{coupler(1to}N\text{)}}, Z_1 = \frac{(\omega L_1)^2}{Z_2}, Z_2 = Z_p + r_p \tag{20}$$

where Z_{in}, Z_1, Z_2, and Z_p are resistive according to (5)–(8). As the load increases, the efficiency first increases and then decreases. When the number of output unit N increases, the maximum efficiency and the optimal load increase. Specifically, when $N = 10$, the maximum ac-to-ac efficiency is 94.69% at

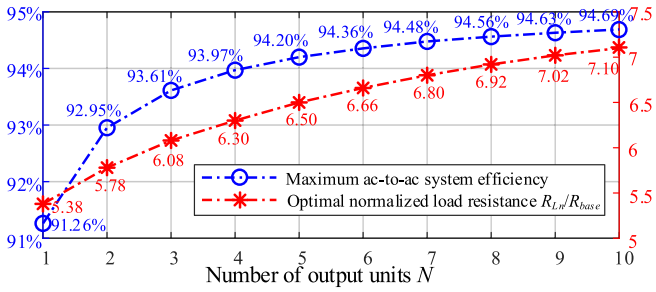

Fig. 10. Calculated maximum AC-to-AC efficiency and optimal normalized load resistance *vs*. number of output units *N*.

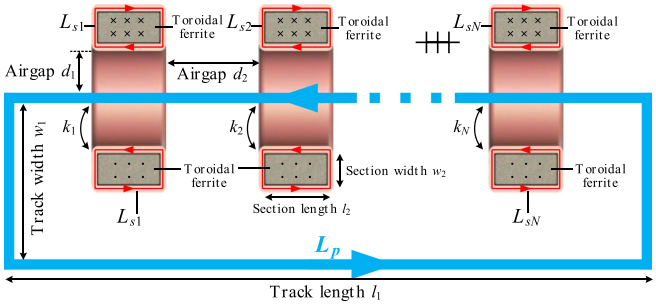

Fig. 11. Conceptual configuration of the magnetic coupler structure.

TABLE I
DIMENSIONAL PARAMETERS OF MAGNETIC COUPLERS

Primary coil		Secondary coils			
l_1	w_1	l_2	w_2	d_1	d_2
0.8 m	0.2 m	16 mm	8 mm	8 mm	130 mm

4.4 W output power for each unit, which is sufficient to power a gate drive of a power device.

Fig. 10 summarizes the calculated ac-to-ac maximum efficiency and optimal normalized load. As *N* increases, the maximum efficiency and optimal load resistance increase.

III. DESIGN OF A WEPUS WITH TEN OUTPUTS

A. Magnetic Coupler Analysis

Fig. 11 shows the magnetic coupler configuration. The primary transmitter track is coupled with coaxially distributed pick-up receiver coils through the center, which are consistent for the sake of simplicity. The track length l_1 is relatively longer than its width w_1. Each toroidal pick-up coil has an identical air gap d_1 to the central track. The distances between adjacent coils are also identical, denoted as airgap d_2. Reference directions of currents (cyan and red lines for primary and secondary coils) and magnetic flux are labeled.

All pick-up coils are fabricated using toroidal ferrite with Litz wire. For compactness, components are integrated on a printed circuit board (PCB), including receiver coils, capacitors, and rectifiers, as shown in Fig. 12. Based on the coupler dimensions in Table I, a three-dimensional (3-D) model of ten receivers is shown in Fig. 13.

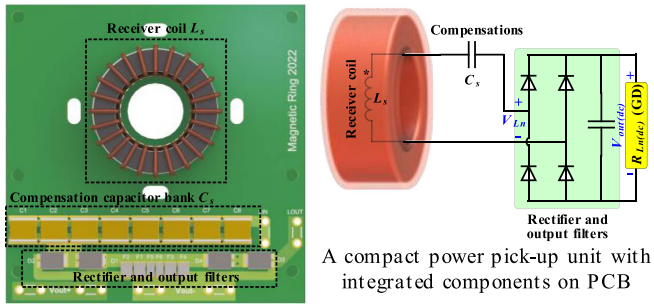

A compact power pick-up unit with integrated components on PCB

Fig. 12. PCB layout of a compact power pick-up unit, including receiver coil, compensation bank, output rectifiers and DC loads $R_{Ln(dc)}$ (Gate Drive).

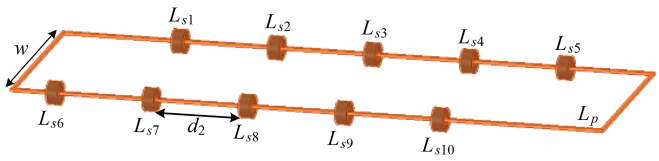

Fig. 13. Maxwell simulated model of the magnetic coupler with ten receivers.

TABLE II
MAXWELL SIMULATED COUPLING COEFFICIENTS

Main couplings (k_1~k_{10})	Cross couplings
0.24075–0.24079	4.96×10^{-12}–2.41×10^{-7}

TABLE III
CROSS-COUPLING COEFFICIENT WITH VARYING DISTANCE

Distance d_2	40 mm	60 mm	80 mm	100 mm	130 mm
Maximum cross-coupling	7.42×10^{-6}	2.38×10^{-6}	8.19×10^{-7}	5.60×10^{-7}	2.41×10^{-7}

The main couplings between L_p and L_{s1}~L_{s10} are represented by k_1~k_{10}. Table II gives coupling coefficients extracted from Maxwell. The main coupling coefficients are around 0.241.

Cross-coupling is an important factor that affects the CV characteristic of the IPT system. In this design, due to the utilization of toroidal ferrite ring in each pick-up unit, the flux is concentrated in each individual core which can significantly reduce the cross-coupling. To further explore the effect of coil distance on the cross-coupling, more simulations are conducted in Maxwell at different distances from 40 mm to 130 mm, whose results are given in Table III. It indicates that even if the distance is reduced to 40 mm, the maximum cross-coupling coefficient is still only 7.42×10^{-6}, which is ignorable compared to the main coupling coefficients around 0.241. The influence of cross couplings is therefore negligible in the circuit analysis.

Meanwhile, it is worth noting that the actual coil distance in this design is regulated by the size of each SSCB submodule instead of the IPT requirements, which will be demonstrated in Section V-A.

Moreover, it also needs to be emphasized that the magnetic core saturation needs to be considered in practical design. The receiving side current of each pick-up unit should not exceed a particular value to prevent magnetic core saturation. For the

TABLE IV
SYSTEM PARAMETERS FOR LTSPICE SIMULATION

Parameter	Value	Parameter	Value
V_{dc}	18 V	C_1	159.6 nF
N	10	C_{s1}~C_{s10}	3.42 nF
f	230 kHz	k_1~k_{10}	0.241
L_1	3 μH	Q_1	50
L_p	3 μH	Q_p	50
L_{s1}~L_{s10}	140 μH	Q_{s1}~Q_{s10}	100

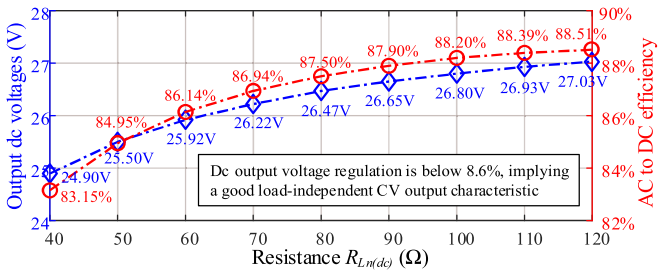

Fig. 14. LTspice-simulated results of DC output voltages and system AC-to-DC efficiency, validating load-independent CV output characteristic.

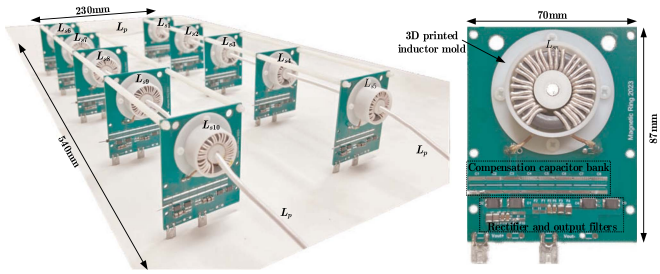

Fig. 15. WEPUS APS system prototype with ten outputs.

TABLE V
DESIGN PARAMETERS OF THE WEPUS APS PROTOTYPE

Parameter	Value	Parameter	Value
V_{dc}	18V	k_1~k_{10}	0.22
f	230 kHz	Q_1	65
L_1	3.36 μH	Q_p	102
C_1	129.3 nF	Q_{s1}~Q_{s10}	450
L_p	3.25 μH	N	10
L_{s1}	145 μH	C_{s1}	3.22 nF
L_{s2}	145 μH	C_{s2}	3.25 nF
L_{s3}	140 μH	C_{s3}	3.39 nF
L_{s4}	141 μH	C_{s4}	3.32 nF
L_{s5}	144 μH	C_{s5}	3.29 nF
L_{s6}	143 μH	C_{s6}	3.25 nF
L_{s7}	142 μH	C_{s7}	3.29 nF
L_{s8}	139 μH	C_{s8}	3.39 nF
L_{s9}	140 μH	C_{s9}	3.39 nF
L_{s10}	139 μH	C_{s10}	3.39 nF

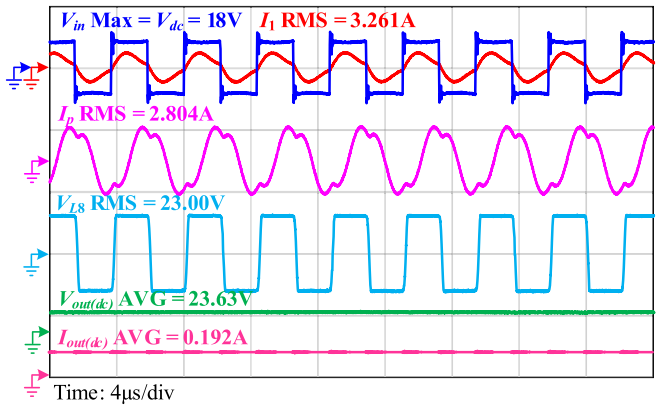

Fig. 16. Experimental waveform at $P_{\mathrm{out\_total}} = 47.1$ W, showing the 8 output unit.

APS application, it is usually not a serious concern since the output current is very low due to the low power consumption of gate drivers.

B. Circuit Simulation Results

Table IV gives the parameters for a circuit simulation in LTspice to verify the load-independent CV output. The rectifier and dc load in this simulation follow the configuration in Fig. 12. To simplify the analysis, the parameters of ten output units and their loads are identical.

Fig. 14 shows the simulated results of output DC voltages and efficiency variations with load. As load resistance spans from 40 to 120 Ω, the output voltage regulation rate is below 8.6%, implying a good load independent CV output. The simulated ac-to-dc efficiency is roughly 6% lower than the ac-to-ac efficiency calculated in Fig. 9, which is mainly due to power losses of rectifiers on the ten output units.

IV. EXPERIMENT VALIDATION I: WEPUS TESTING

A. Hardware Description

Fig. 15 shows an implemented WEPUS prototype with ten outputs. It includes a single-turn primary track coil and ten coupled receiver coils. The primary track has dimensions of 230 mm × 540 mm, which is implemented by 0.03 mm × 6000 strands litz wire. The secondary toroidal coil has inside and outside diameters of 16mm and 32mm, respectively with a height of 16 mm. The receiving coil is implemented by 0.1 mm × 100 strands litz wire. A 3-D printed holder is fabricated to fix the toroidal coil. The primary track goes through the central hole of the 3-D fixture, which reliably isolates transmitting and receiving sides. The PCB-based power pick-up unit achieves a compact size of 87 mm × 70 mm.

Design parameters for experimental validation are given in Table V. At the upstream side, a dc source and an inverter are used to provide 230 kHz excitation. The rectified dc outputs are connected to ten identical load resistors.

B. Experimental Validation of the WEPUS

Figs. 16 and 17 show the measured waveforms of the prototype. At the input side, both ZPA and zero voltage switching (ZVS) are realized. Due to consistency, only one unit (eight) is presented as an example, and the waveforms of other units are similar. When the total output power is 47.1 W, the output dc voltage is 23.63 V on the eighth unit. When the total output

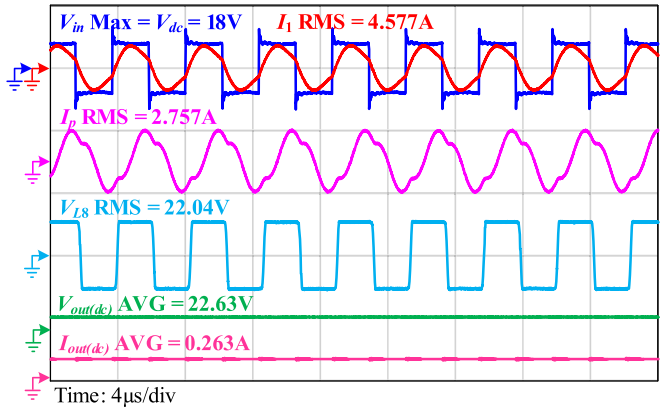

Fig. 17. Experimental waveform at $P_{\text{out\_total}} = 60.9$ W, showing the eighth output unit.

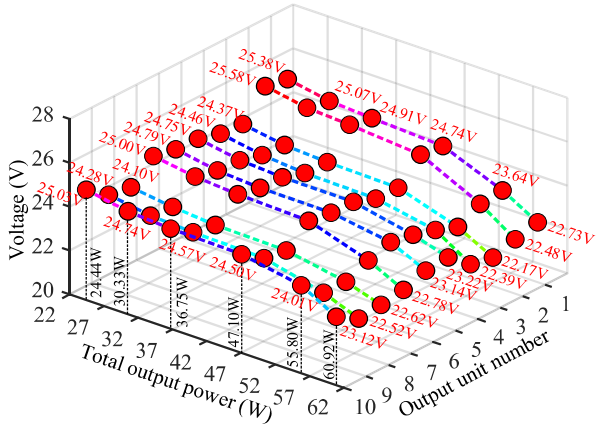

Fig. 18. Experimental results summarizing the WEPUS output voltages with different output power at ten units, respectively.

TABLE VI
OUTPUT VOLTAGE REGULATION RATES

VR_1	VR_2	VR_3	VR_4	VR_5
11.66%	13.79%	9.92%	9.25%	6.59%
VR_6	VR_7	VR_8	VR_9	VR_{10}
7.13%	9.75%	6.54%	7.82%	8.26%

power increases to 60.9 W, the voltage slightly reduces to 22.63 V.

Fig. 18 shows experimental results of ten dc output voltages. When the total output power increases from 22.44 to 60.92 W, all ten output voltages are maintained around 24V. To quantify fluctuation, the voltage regulation (VR) rate is defined as

$$\text{VR}_n = \frac{V_{\text{out\_}n(dc)}|_{P_{\text{out}}=24.44\text{W}} - V_{\text{out\_}n(dc)}|_{P_{\text{out}}=60.92\text{W}}}{V_{\text{out\_}n(\text{dc})}|_{P_{\text{out}}=60.92\text{W}}} \times 100\%. \tag{21}$$

Table VI gives calculated results of VR of ten units, which indicates a good load-independent CV output.

Fig. 19 further shows the measured dc-to-dc efficiency from the dc source input to the ten rectified outputs. It needs to be mentioned that the power loss in all the circuit components are considered, including the coils, compensation capacitors, inverter, and rectifiers. The system has a wide range of high

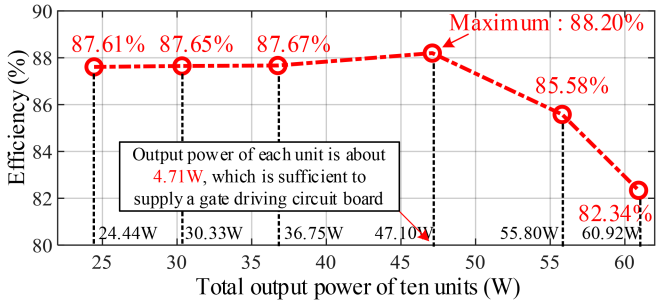

Fig. 19. Measured DC-to-DC efficiency versus total output power of the ten units.

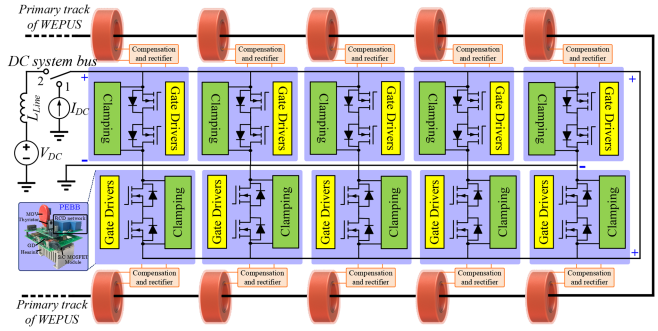

Fig. 20. System configuration of an SSCB consisting of ten paralleled submodule PEBBs, powered by WEPUS with load-independent outputs for gate-drives.

efficiency, and the measurement shows a peak value of 88.2% at 47.1 W, indicating an average of 4.71 W for each unit, which is enough to power the gate driver of an SSCB.

C. Comparative Study

Table VII gives a comparative investigation of the proposed WEPUS against other literature of APS systems, where compensation type, number of compensation components, number of outputs, efficiency, APS unit size, and application are considered to highlight the uniqueness of this article. It is worth noting that other than traditional IPT applications, the gate-drive auxiliary supply generally has low requirements on power transfer capability while compactness is more attractive. Therefore, the size of APS unit, instead of power level or power density, is used for the comparative study in this section.

As noted in Table VII, the proposed *LCL-S* compensated WEPUS APS system has unique contributions. It achieves the greatest number of output circuits with a reduced number of resonance components. A high efficiency is also realized with a compact APS configuration, which provides superior design guidelines for SiC MOSFETs gate-drive supply in modular dc SSCBs compared to the existing pieces of literature.

V. EXPERIMENTAL VALIDATION II: WEPUS POWERED SSCB

A. System Description of a Modular SSCB

Fig. 20 shows the system configuration of an SSCB powered by the proposed WEPUS. The SSCB modularity follows the

TABLE VII
COMPARISON OF EXISTING APS SYSTEMS

Description	Compensation type	Compensation components #	Output circuits #	Efficiency	APS unit size	Application
[11]	S-SP	3*N*	*N*=6	88.1%	160 mm×160 mm	IGBT gate-drive
[12]	S-S	8	2	66.7%	ϕ270 mm	Post insulators in substations
[14]	S-CLC	4*N*	*N*=6	91.0%	160 mm×160 mm	IGBT gate-drive
[21]	S-S	*N*+1	*N*=3	66.6%	60 mm×100 mm	N/A
[22]	S-S	*N*+4	*N*=6	71.0%	ϕ200 mm	Battery cell equalization
[26]	LCC-S	*N*+3	*N*=2	86.0%	37 mm×37 mm	SiC MOSFET gate-drive
This work	LCL-S	*N*+2	*N*=10	88.2%	70 mm×87 mm	SiC MOSFET gate-drive

TABLE VIII
SYSTEM PARAMETERS OF MODULAR DC SSCB TESTING

Parameter	Value	Parameter	Value
V_{DC}	1.33 kV	S_m Gate Drive	UCC21750
I_{DC}	400 A	SCR	TYN50W-1600
I_{fault}	2000 A(5×)	SCR Gate Drive	1ED3123MU12
L_{Line}	16 µH, 300 µH	MOV	V751HA40
S_m	CAB450M12XM3	R_{static}	10 MΩ
Parallel #	10	R_a	20 kΩ

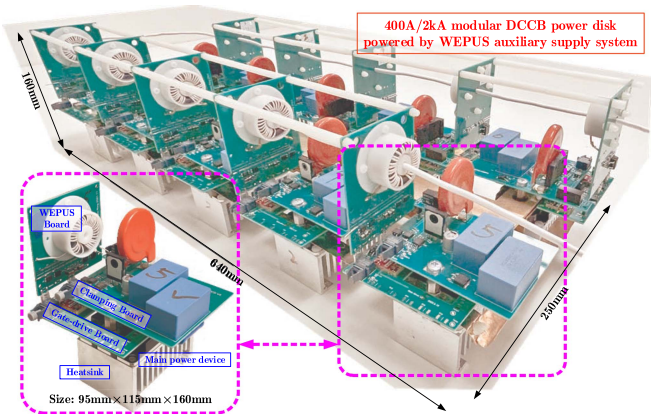

Fig. 21. Modular SSCB prototype powered by the proposed WEPUS.

structure presented in [29], ten submodules are connected in parallel in this example to handle high current. Each submodule consists of a WEPUS, a main switch in a half-bridge form, a control interface, a voltage clamping unit to absorb the transient energy, and a thermal management unit, forming a PEBB.

Table VIII provides circuit parameters of the SSCB aiming at medium voltage applications. The part numbers of key components are also shown. The 1.2 kV half-bridge SiC MOSFET module CAB450M12XM3 is used in this prototype. The dc rating voltage is 1.33 kV, and the dc rating current is 400 A. The targeted fault current magnitude is 2 kA, which is five times of its nominal value.

Fig. 21 shows the implemented SSCB prototype, including the main conduction circuit supported by the proposed WEPUS. Ten parallel PEBBs can support the current ratings while maintaining a low conduction loss and high efficiency. The resulting dimension is 640 mm × 250 mm × 160 mm, and the power density can reach 20.8 kW/L.

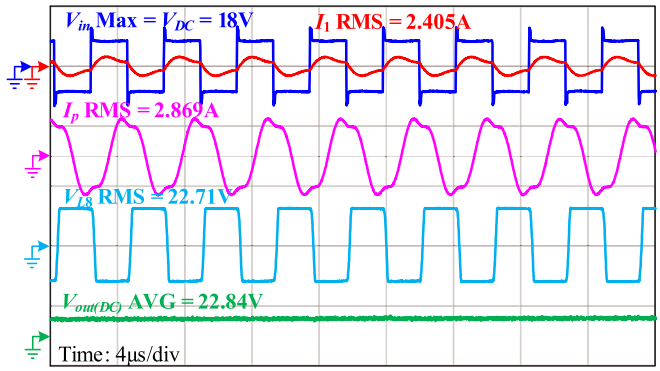

Fig. 22. Experiment results of the WEPUS when powering ten gate drives of the SSCB. $P_{\text{in\_total}} = 39.7$ W, showing DC outputs at eighth unit.

Since the key point presented in this design is the modularity of the SSCB, ten submodules are implemented in the eventual SSCB prototype in Fig. 21, in which each submodule has its own individual WEPUS board, gate-drive board, and clamping board. The size of each submodule is 95 mm × 115 mm × 160 mm. It needs to be emphasized that total number of submodules can be tuned based on actual operation ratings. That is, it is acceptable to have less gate-drives if the SSCB is specified for a lower rating, which results in more compact designs.

For the sake of disambiguation, it is noted that the proposed WEPUS APS system is only part of the total SSCB system presented in Fig. 21. As shown in Fig. 15, each WEPUS auxiliary supply unit has a relatively compact dimensions of 70 mm × 87 mm, which is applicable for the SSCB.

B. WEPUS Powering Test for SSCB Turn On

The implemented WEPUS is used to power on the gate driver of the SSCB, which is able to supply power for ten parallel submodules simultaneously.

Fig. 22 shows measured WEPUS waveforms when powering gate driver loads in the SSCB. It is similar to Figs. 16 and 17, and the ZPA and ZVS are realized as expected. At the output side, both ac output and rectified dc output are measured. The total input power of the WEPUS is 39.6 W, while the output dc voltage is 22.84 V on the 8th unit, which matches the resistor load test results in Section III. Meanwhile, the efficiency of the WEPUS is also measured as 87.66%, which is a high enough performance for the real application.

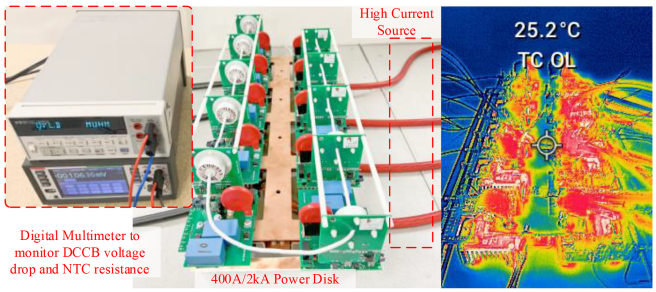

Fig. 23. Experiment setup of a 400 A/1 h SSCB continuous conduction test.

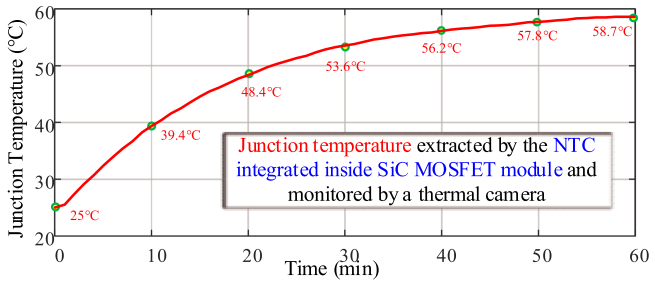

Fig. 24. Experimentally measured junction temperature of the SiC module in the modular DC SSCB.

C. Continuous Test of WEPUS Under 400 A/1hour Condition

During the working process of an SSCB, it needs to conduct continuous high current. In order to test the continuous capability of the SSCB, including its WEPUS unit, the rated 400 A current experiment is performed, and the test time is up to 1-h to make sure the SSCB system reaches thermal steady state, and the proposed WEPUS is able to provide continuous power reliability.

Fig. 23 shows the continuous current hardware test bench. A high current dc source is adopted to supply 400 A CC for the SSCB. An internally packaged NTC inside the power module is used to measure the main power switch junction temperature. The thermal image after 1-h continuous running shows that there is no significant temperature rise for the entire setup, including the power module and the developed WEPUS. It must be clarified that the surface temperature of both power module and magnetic core are within a safe range. A digital multimeter DMM6500 is used to measure the conduction voltage drop across the SSCB with a high precision of 100nV, which ensures the measurement accuracy.

Fig. 24 shows the measured junction temperature from NTC of the MOSFET module. The steady-state junction temperature is limited below 59 °C even after 1-h conduction of 400 A rated current, validating the effectiveness of the passive cooling and busbars in the long-term operation.

Fig. 25 shows the DMM measured main switch voltage drop. The steady-state voltage drop of main switches is only 0.265 V after 1-h conduction. Then, the SSCB efficiency under different dc system voltage levels is calculated and shown in Fig. 26 based on

$$\eta_{\mathrm{SSCB}} = (1 - V_{\mathrm{drop}}/V_{\mathrm{DC}}) \times 100\%. \tag{22}$$

It indicates that this design has successfully achieved a record-breaking 99.98% efficiency at a desired 1.33 kV dc system voltage rating. Here, it is emphasized that the SSCB efficiency is different from the WEPUS efficiency.

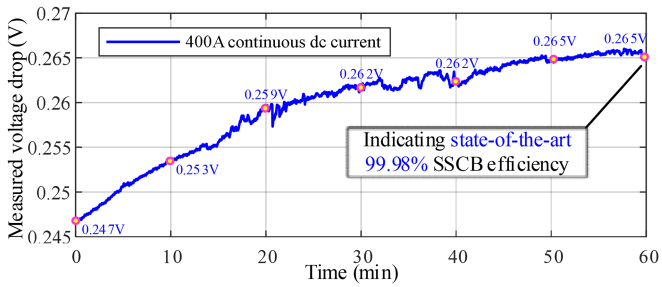

Fig. 25. DMM measured voltage drop of the SSCB main power switch.

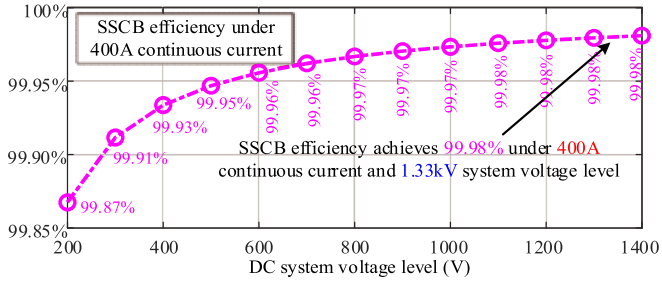

Fig. 26. SSCB efficiency versus DC system voltage level.

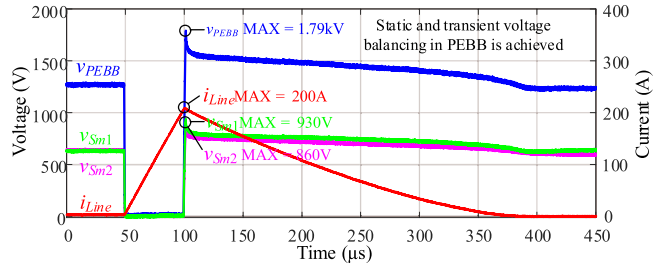

Fig. 27. Transient test of a submodule PEBB under 1.33 kV/200 A interruption.

D. Transient Test of WEPUS Under Fault Interruption Test

The implemented WEPUS also needs to support the fault interruption test of the SSCB, which ensures that the SSCB is well powered when disconnects a fault current. During experiments, a single submodule PEBB is tested, and then the entire SSCB test follows.

Fig. 27 shows the 1.33 kV/200 A transient interruption test of a submodule PEBB to emulate a fault protection scenario. During the test process, the dc-bus voltage is charged to the rated value, 1.33 kV. Then, the SSCB turns on to emulate a short-circuit fault. Once the fault current increases to 200 A, the SSCB is triggered

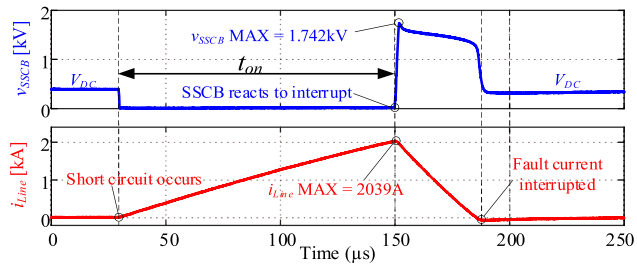

Fig. 28. Transient test of the entire SSCB under 2 kA interruption.

to turn OFF. Fig. 27 shows that the SSCB is effective to turn off the fault and reduce the line current to zero after about 260 μs of the fault. In addition, the voltages across the half-bridge module of the main switch is also measured, showing a good steady-state and transient voltage balancing performance of the SSCB.

Fig. 28 shows a further experiment to validate the transient performance of the WEPUS to support 2 kA current interruption of the entire 10 submodules paralleled SSCB. In this case, the DC voltage is 380V, and the SSCB turns on for 120 μs to generate a fault current up to 2.039 kA. Then, the SSCB turns OFF, and the clamping voltage increases to 1.742 kV to reduce the line current to zero timely. During the current interruption transient, the output dc voltage of the WEPUS is monitored, and there is no significant voltage fluctuation. It validates that the implemented APS system is effective to provide sufficient power to the SSCB application in both continuous and transient operations.

VI. Conclusion

This article aims to design a load-independent CT-based WEPUS system with CV outputs to power medium-voltage devices' gate drives in an SSCB, which provides a complete modularity for each submodule of the SSCB. The working principle of the WEPUS system is explained in detail, with the modeling of output voltage and efficiency analysis with parasitic resistances.

A prototype of a single-turn transmitter with ten receivers is implemented to verify the proposed design. Experimental results validate the independent CV outputs, and the efficiency can reach 88.20% with ten loads and a total output power of 47.1 W. Then, the WEPUS is integrated into a real SSCB prototype with ten submodules in parallel. The practical operation efficiency of the WEPUS reaches 87.66%.

The WEPUS powered SSCB prototype is then tested for both: 400 A/1 h continuous conduction to validate its long-term operation and 2 kA fault current interruption to verify its fault clearance capability. A record-breaking 99.98% steady-state efficiency of the SSCB is successfully achieved. A fast speed of fault interruption capability of 2 kA is realized. This article is expected to provide a point of reference for WEPUS design in modular SSCB and other applications.

Acknowledgment

The information, data, or work presented herein was funded in part by the Advanced Research Projects Agency-Energy (ARPA-E), U.S. Department of Energy, under Award Number DE-AR0001114 in the BREAKERS program monitored by Dr. Isik Kizilyalli. The views and opinions of authors expressed herein do not necessarily state or reflect those of the United States Government or any agency thereof.

References

[1] N. Hou, L. Ding, P. Gunawardena, T. Wang, Y. Zhang, and Y. W. Li, "A partial power processing structure embedding renewable energy source and energy storage element for islanded DC microgrid," *IEEE Trans. Power Electron.*, vol. 38, no. 3, pp. 4027–4039, Mar. 2023, doi: 10.1109/TPEL.2022.3221349.

[2] S. Zhang, M. Zhou, and G. Li, "Applying power margin tracking droop control to flexible operation in multi-terminal DC collector systems of renewable generation," *CSEE J. Power Energy Syst.*, vol. 7, no. 6, pp. 1176–1186, Nov. 2021.

[3] H. Jain, B. Mather, A. K. Jain, and S. F. Baldwin, "Grid-Supportive Loads—A new approach to increasing renewable energy in power systems," *IEEE Trans. Smart Grid*, vol. 13, no. 4, pp. 2959–2972, Jul. 2022, doi: 10.1109/TSG.2022.3153230.

[4] X. Zhang, X. Shao, Y. Fu, X. Zhao, and G. Jiang, "Transient voltage recovery control and stability criterion of VSC-Based DC power grid," *IEEE Trans. Power Syst.*, vol. 36, no. 4, pp. 3496–3506, Jul. 2021, doi: 10.1109/TPWRS.2020.3044360.

[5] J. Zeng, W. Qiao, L. Qu, and Y. Jiao, "An isolated multiport DC–DC converter for simultaneous power management of multiple different renewable energy sources," *IEEE J. Emerg. Sel. Topics Power Electron.*, vol. 2, no. 1, pp. 70–78, Mar. 2014.

[6] Q. Huo et al., "Review of DC circuit breaker application," *Elect. Power Syst. Res.*, vol. 209, 2022, Art. no. 107946.

[7] R. Rodrigues, Y. Du, A. Antoniazzi, and P. Cairoli, "A review of solid-state circuit breakers," *IEEE Trans. Power Electron.*, vol. 36, no. 1, pp. 364–377, Jan. 2021.

[8] P. Channegowda, B. Liu, B. Riar, and X. Wu, "Testing solid state DC circuit breakers for electrified aircraft applications," in *Proc. IEEE Transp. Electrific. Conf. Expo*, 2022, pp. 1123–1127, doi: 10.1109/ITEC53557.2022.9813998.

[9] T. Takamori, K. Wada, W. Saito, and S. -i. Nishizawa, "Paralleled SiC MOSFETs DC circuit breaker with SiC MPS diode as avalanche voltage clamping," in *Proc. IEEE Appl. Power Electron. Conf. Expo.*, 2022, pp. 225–229.

[10] I. V. Raghavendra, S. N. Banavath, C. N. M. Ajmal, and A. Ray, "Modular bidirectional solid-state DC circuit breaker for next-generation electric aircrafts," *IEEE J. Emerg. Sel. Topics Power Electron.*, vol. 10, no. 5, pp. 5486–5497, Oct. 2022.

[11] C. Cheng, Z. Zhou, W. Li, J. Lu, Z. Deng, and C. C. Mi, "Long-distance wireless power transfer system powering multiple loads with constant voltage outputs using S-SP compensation," *IET Power Electron.*, vol. 13, pp. 1729–1734, 2020.

[12] P. Gu, Y. Wang, Z. Liu, J. Mai, T. Li, and D. Xu, "Analysis and design of Long-range IPT system with Multi-load CV characteristics based on cylindrical solenoid coupler," *IEEE Trans. Ind. Appl.*, vol. 59, no. 2, pp. 2363–2373, Mar./Apr. 2023, doi: 10.1109/TIA.2022.3233561.

[13] W. Chen, K. Ji, Y. Zhang, and J. Wang, "Design and analysis of multi-load inductive power transfer system using bilateral-excitation scheme," *IEEE Trans. Ind. Inform.*, vol. 18, no. 1, pp. 365–374, Jan. 2022, doi: 10.1109/TII.2021.3076177.

[14] C. Cheng, C. Wang, Z. Zhou, W. Li, Z. Deng, and C. C. Mi, "Repeater coil-based wireless power transfer system powering multiple gate drivers of series-connected IGBTs," *IET Power Electron.*, vol. 13, pp. 1722–1728, 2020.

[15] C. Cheng, Z. Zhou, W. Li, Z. Deng, and C. C. Mi, "A power relay system with multiple loads using asymmetrical coil design," *IEEE Trans. Ind. Electron.*, vol. 68, no. 2, pp. 1188–1195, Feb. 2021.

[16] X. Xie, C. Xie, and L. Li, "Wireless power transfer to multiple loads over a long distance with load-independent constant-current or constant-voltage output," *IEEE Trans. Transp. Electrific.*, vol. 6, no. 3, pp. 935–947, Sep. 2020.

[17] C. Zhang, D. Lin, N. Tang, and S. Y. R. Hui, "A novel electric insulation string structure with high-voltage insulation and wireless power transfer capabilities," *IEEE Trans. Power Electron.*, vol. 33, no. 1, pp. 87–96, Jan. 2018, doi: 10.1109/TPEL.2017.2706221.

[18] B. Luo, D. Ma, W. Han, and J. Liu, "Extensible low-profile coplanar wireless power transfer system for multiload applications with load-independence constant current output," *IEEE Trans. Ind. Electron.*, vol. 69, no. 11, pp. 11187–11197, Nov. 2022.
[19] Y. Wang, Z. Dongye, R. Kheirollahi, H. Zhang, S. Zheng, and F. Lu, "Review of load-independent constant-current and constant-voltage topologies for domino-type multiple-load inductive power relay system," *IEEE J. Emerg. Sel. Topics Ind. Electron.*, vol. 3, no. 2, pp. 199–210, Apr. 2022.
[20] S. Sun, B. Zhang, C. Rong, X. Shu, and Z. Wei, "A multireceiver wireless power transfer system using self-oscillating source composed of zero-voltage switching full-bridge inverter," *IEEE Trans. Ind. Electron.*, vol. 69, no. 3, pp. 2885–2895, Mar. 2022.
[21] M. Fu, H. Yin, M. Liu, Y. Wang, and C. Ma, "A 6.78 MHz multiple-receiver wireless power transfer system with constant output voltage and optimum efficiency," *IEEE Trans. Power Electron.*, vol. 33, no. 6, pp. 5330–5340, Jun. 2018.
[22] M. Liu, M. Fu, Y. Wang, and C. Ma, "Battery cell equalization via megahertz multiple-receiver wireless power transfer," *IEEE Trans. Power Electron.*, vol. 33, no. 5, pp. 4135–4144, May 2018, doi: 10.1109/TPEL.2017.2713407.
[23] M. Fu, T. Zhang, C. Ma, and X. Zhu, "Efficiency and optimal loads analysis for multiple-receiver wireless power transfer systems," *IEEE Trans. Microw. Theory Techn.*, vol. 63, no. 3, pp. 801–812, Mar. 2015, doi: 10.1109/TMTT.2015.2398422.
[24] Y. -J. Kim, D. Ha, W. J. Chappell, and P. P. Irazoqui, "Selective wireless power transfer for smart power distribution in a miniature-sized multiple-receiver system," *IEEE Trans. Ind. Electron.*, vol. 63, no. 3, pp. 1853–1862, Mar. 2016.
[25] W. Xu and A. Q. Huang, "15 kV/50 A SiC AC switch based on series connection of 1.7kV MOSFETs," in *Proc. IEEE Energy Convers. Congr. Expo.*, 2022, pp. 1–6.
[26] J. Hu, J. Wang, R. Burgos, B. Wen, and D. Boroyevich, "High-Density current-transformer-based gate-drive power supply with reinforced isolation for 10-kV SiC MOSFET modules," *IEEE J. Emerg. Sel. Topics Power Electron.*, vol. 8, no. 3, pp. 2217–2226, Sep. 2020, doi: 10.1109/JESTPE.2019.2943742.
[27] X. Cui et al., "Analysis methodology for differential mode interference in energy supply system of hybrid DC breaker," *IEEE Trans. Electromagn. Compat.*, vol. 61, no. 6, pp. 1967–1978, Dec. 2019, doi: 10.1109/TEMC.2019.2952247.
[28] Y. Wang, S. Zhao, H. Zhang, and F. Lu, "High-Efficiency bilateral S–SP compensated multiload IPT system with constant-voltage outputs," *IEEE Trans. Ind. Inform.*, vol. 18, no. 2, pp. 901–910, Feb. 2022.
[29] S. Zhao, R. Kheirollahi, Y. Wang, H. Zhang, and F. Lu, "Economic implementation of 99.98% efficiency in natural-cooling modular MVDC SSCBs," *IEEE Trans. Ind. Electron.*, vol. 70, no. 9, pp. 9515–9526, Sep. 2023, doi: 10.1109/TIE.2022.3212404.

Shuyan Zhao (Student Member, IEEE) received the B.S. degree from Wuhan University, Wuhan, China in 2017, and the M.S. degree from China University of Mining and Technology, Xuzhou, China in 2020, both in electrical engineering. He is currently working toward the Ph.D. degree in electrical engineering with Drexel University, Philadelphia, PA, USA.

His research interests include application of high voltage wide bandgap semiconductors, dc circuit breakers and wireless power transfer technology.

Mr. Zhao was the recipient of IEEE PELS ITEC Best Student Paper Award in 2022, IEEE IAS Renewable and Sustainable Energy Conversion Systems Committee Meeting First Prize Paper Award in 2022, and IEEE PELS ECCE Student Project Demonstration Award in 2022.

Yao Wang (Student Member, IEEE) received the B.S. and M.S. degrees in electrical engineering from Northwestern Polytechnical University, Xi'an, China, in 2017 and 2020, respectively. He is currently working toward the Ph.D. degree in electrical engineering with Drexel University, Philadelphia, PA, USA.

His research interest focuses on wireless power transfer technology and resonant converter.

Reza Kheirollahi (Student Member, IEEE) received the M.S. degree from Tarbiat Modares University, Tehran, Iran, in 2016, and the Ph.D. degree from the Drexel University, Philadelphia, PA, USA, in 2023, both in electrical engineering.

His research topic focuses on power electronics, dc circuit breakers, wireless power transfer technology, dc and ac microgrids, optimization algorithms, and software and hardware embedded systems.

Yang Zheng is currently working toward the B.S. degree in mechanical engineering with the Drexel University, Philadelphia, PA, USA.

She was an undergraduate student Research Assistant in electrical engineering with the Drexel University, Philadelphia, PA, USA, in 2023. Her current research topic focuses on industrial design of power electronics converters and wireless power transfer technology.

Zilong Zheng received the B.A. degree in psychology and the B.A. degree in business from Hope College, Holland, MI, USA, in 2014, and the master's degree in entrepreneurship from the University of Pennsylvania, Philadelphia, PA, USA, in 2019. He is currently working toward the Ph.D. degree in electrical engineering with Drexel University, Philadelphia, PA, USA.

His research interests focus on high-power wireless charging for various applications, solid-state circuit breakers, power electronics, and the utilization and commercialization of these technologies in a variety of industry settings.

Shervin Salehi Rad received the M.S. degree in power electronics engineering from Tarbiat Modares University, Tehran, Iran, in 2017. He is currently working toward the Ph.D. degree in electrical engineering with Drexel University, Philadelphia, PA, USA.

His research interests inlcude processor-in-the-loop testing of power electronics converters, the application of high-voltage wide bandgap semiconductors, and wireless power transfer technology.

Hua Zhang (Member, IEEE) received B.S., M.S., and Ph.D. degrees in electrical engineering from Northwestern Polytechnical University, Xi'an, China, in 2011, 2014, and 2017, respectively.

She is currently an Assistant Professor with Rowan University, Glassboro, NJ, USA. Her research focuses on high voltage power conversion technology for electric vehicles and power grid applications.

Fei Lu (Member, IEEE) received the B.S. and M.S. degrees from Harbin Institute of Technology, Harbin, China, in 2010 and 2012, respectively, and the Ph.D. degree from the University of Michigan, Ann Arbor, Michigan, USA, in 2017, all in electrical engineering.

He is currently an Assistant Professor with the Department of Electrical and Computer Engineering, Drexel University, Philadelphia, PA, USA. His research topic focuses on power electronics and the application of electric vehicle charging.